Nanoscale Advances

PAPER

View Article Online
View Journal | View Issue

Cite this: *Nanoscale Adv.*, 2024, **6**, 5133

Silver decorated nickel oxide nanoflake/carbon nanotube nanocomposite as an efficient electrocatalyst for ethanol oxidation

Nada Gamal ElSayed,[a] Ahmed A. Farghali,[a] Waleed M. A. El Rouby [a] and Mai F. M. Hmamm *[b]

The higher energy density and lesser toxicity of ethanol compared to methanol make it an ideal combustible renewable energy source in fuel cells. Finding suitable cost-effective electrocatalysts that can oxidize ethanol in ethanol-based fuel cells is a major challenge. With their high catalytic activity and stability in alkaline media, transition metal-based catalysts are ideal candidates for alkaline direct ethanol fuel cells. Nickel-based nanomaterials and composites exhibit high electrocatalytic activity, which makes them predominant candidates for the electrochemical oxidation of ethanol. In this study, the electrocatalytic activity of a nickel oxide flower-like structure was explored. Forming a nanocomposite of NiO in combination with carbon nanotubes (CNTs), NiO/CNTs, as a substrate led to an increase in the stability of the electrocatalyst in alkaline media. Furthermore, the electrocatalytic activity of the NiO/CNT nanocomposite was greatly enhanced by decorating the surface with different ratios of silver (Ag). Ag/NiO/CNT composites with different Ag ratios, namely, 25% and 50% by weight, were studied. The Ag 25%/NiO/CNT weight ratio showed a maximum ethanol conversion. At an ethanol concentration of 300 mM, the electrochemical oxidation current density was found to be 57.1 ± 0.2 mA cm^{-2} for the 25% by weight Ag ratio, with a five-fold increase in the current density (compared to NiO/CNTs (10 ± 0.34 mA cm^{-2})). Furthermore, the nanocomposite synthesized here (Ag 25%/NiO/CNTs) showed a significantly higher energy conversion (current per ethanol concentration) rate compared to other reported NiO-based catalysts. These results open real opportunities for designing high efficiency ethanol fuel cell catalysts.

Received 5th July 2024
Accepted 8th August 2024

DOI: 10.1039/d4na00549j

rsc.li/nanoscale-advances

1. Introduction

Development of clean energy alternatives represents the cornerstone of the current world economy; in particular, finding energy sources that are more eco-friendly and overcome the challenging global warming caused by the predominant fossil fuel-based energy resources is becoming vital.[1–4] Direct alcohol fuel cells (DAFCs) have attracted enormous interest owing to their high energy conversion rate, facile storage, transportability at ambient conditions, and less pollution.[5,6] Direct methanol fuel cells (DMFCs) represent the most advanced form of DAFCs owing to their high energy density of ~6 kW h kg^{-1} together with their longer cell lifetime, low emission of pollutants, low cost of methanol, facile transportation and storage and ease of operation.[7] Although DMFCs offer attractive operational advantages as a power source, these fuel cells suffer from some problems such as slow methanol oxidation kinetics. Moreover, other limitations such as anode poisoning with carbon monoxide and alcohol crossover through Nafion membranes decrease the cathode efficiency of these cells.[8,9] In addition, the toxicity of methanol represents a serious concern in handling and transporting DMFCs and might affect their potential in powering portable devices.[10–12] To overcome the toxicity concerns of methanol, direct ethanol fuel cells (DEFCs) have attracted considerable attention as an eco-friendly and non-toxic energy source.[13,14] Using ethanol in fuel cells offers higher energy-density (8.3 kW h kg^{-1}),[15] low toxicity, and safer transport.[16] In addition, ethanol has a lower crossover rate at the cathode, which causes less deterioration of the cathode compared to methanol.[17] The development of electrocatalysts for DEFCs was exclusively dependent on using platinum (Pt)-based catalysts such as PtRu and PtSn.[18,19] Although Pt possesses an exceptional catalytic activity, compared to other metals and materials, it suffers from rapid poisoning caused by strongly adsorbed species that result from the ethanol dissociative adsorption.[20,21]

Over the past few years, transition metal oxides, in particular nickel oxide (NiO) nanostructures have been utilized as

[a]*Materials Science and Nanotechnology Department, Faculty of Postgraduate Studies for Advanced Sciences (PSAS), Beni-Suef University, 62511 Beni-Suef, Egypt*
[b]*Renewable Energy Science and Engineering Department, Faculty of Postgraduate Studies for Advanced Science, Beni-Suef University, 62511 Beni-Suef, Egypt. E-mail: mai.farg@psas.bsu.edu.eg; mai.farge@yahoo.com*

electrode materials in various energy applications.[22,23] For example, NiO nanostructures have been used in supercapacitors, due to their long cycle life, high catalytic activity, and their facile structural and morphological tuning.[24,25] In addition, NiO nanoplatelets have been used as electrode materials for methanol oxidation in DMFC.[26] In the same context, carbon-based nanomaterials have been demonstrated to be one of the most suitable supporting materials in electrocatalysis.[27–29] The fact that carbon-based materials increase the surface area allows for better adsorption of the reactants on the surface of the catalyst and therefore increases the efficiency of the electro-oxidation process. The nature of the supporting carbon and its properties play an important role in the electrocatalytic performance, stability, and reaction kinetics of the catalyst. Carbon nanotubes (CNTs) are considered as excellent supporting electrocatalytic materials owing to their large surface area, stability under extreme conditions and their high conductivity.[30] Furthermore, noble metals, in particular, silver (Ag) have been reported to possess high catalytic activity in many applications.[31] In addition, Ag has been widely used as a supporting co-catalyst to boost the catalytic activity and the electric conductivity of various nanostructured materials and hence increase their catalytic performance.[32]

Here, a NiO flower-like structure was synthesized *via* a hydrothermal method and the electrocatalytic performance of these nanostructures as an electrode material in DEFC application was tested. The effect of using multiwall carbon nanotubes as a supporting material on the electrocatalytic activity and the electrochemical performance of the NiO flower-like structure electrocatalyst was further studied. In addition, the surface of the NiO/CNTs composite has been doped with Ag and the catalytic effect of the Ag on the oxidation of ethanol has also been studied.

2. Materials and methodology

2.1. Materials

Nickel nitrate ($Ni(NO_3)_2 \cdot 6H_2O$), ethanol (C_2H_5OH), ammonia ($NH_3 \cdot H_2O$), carbon nanotubes (CNTs), silver nitrate ($AgNO_3$), sodium borohydride ($NaBH_4$), and potassium hydroxide (KOH), that were used, are of analytical grade and were bought from Aladdin (China). The water used in all the synthesis processes is deionized (DI) water under ambient conditions.

2.2. Synthesis of the nickel oxide (NiO) flower-like structure

The NiO flower-like structure was synthesized using a hydrothermal method according to Yin *et al.*, with slight modifications.[33] Briefly, 2 mmol of $Ni(NO_3)_2 \cdot 6H_2O$ (5.8 g) were dissolved in 50 milliliter (mL) of DI water, and then 10 mL of ethanol (98%) were added to the nickel nitrate solution, under magnetic stirring (solution 1). After 10 minutes, another solution (solution 2) of 8 mmol ammonia ($NH_3 \cdot 6H_2O$) and 42 mL of DI water was slowly added to the $Ni(NO_3)_2 \cdot 6H_2O$ solution, under continuous stirring. The solution mixture was then transferred into a 200 mL Teflon-lined autoclave and heated for 2 hours at 120 °C. The autoclave was left to cool down naturally to room temperature after reaction completion. The sample was centrifuged at 6000 rpm for 10 minutes to collect the product. The collected green solid product was washed with DI water few times, before drying at 70 °C for 2 hours.

2.3. Synthesis of the nickel oxide/carbon nanotube (NiO/CNTs) nanocomposite

Different weight ratios of CNTs to NiO, namely, 20, 10, 5 and 1% were prepared. Multiwall carbon nanotubes were added with different ratios, 300 mg (20%), 150 mg (10%), 75 mg (5%) and 15 mg (1%), to solution 1 (2 mmol of $Ni(NO_3)_2 \cdot 6H_2O$ dissolved in 50 mL of DI water mixed with 10 mL of ethanol (98%)) under magnetic stirring. Then, solution 2 (8 mmol ammonia ($NH_3 \cdot 6H_2O$) and 42 mL of DI water) was added dropwise to solution 1, under stirring at room temperature. The solution mixture was heated up in an autoclave for 2 h at 120 °C. The sample was then precipitated and washed *via* centrifugation a few times with DI water, before oven drying at 70 °C for 2 h.

2.4. Synthesis of the silver decorated NiO/CNTs nanocomposite (Ag/NiO/CNTs)

Ag was assembled on the surface of the NiO/CNTs with different weight percentages (wt%) using the procedures from Bin *et al.*,[34] with slight modifications. The Ag/NiO/CNTs composite of 10, 25 and 50 Ag (wt%) was synthesized by introducing the Ag precursor ($AgNO_3$), followed by the reduction of Ag^+ to Ag atoms using a reducing agent sodium borohydride ($NaBH_4$). Briefly, 10, 25 and 50% (wt) of Ag were prepared by adding 25.47, 63.67 and 127.35 mg, respectively, of silver nitrate ($AgNO_3$) dissolved in 15 mL of DI water to 375 mg of NiO/CNTs, followed by stirring for 2 h at room temperature. The suspension was then centrifuged, followed by DI water washing before drying at 80 °C overnight, enabling all the Ag^+ ions to diffuse into the cavities of NiO/CNTs. Afterwards, 74.9, 187.27 and 374.56 mg, respectively, of $NaBH_4$ were dissolved in 15 mL of DI water, to produce 10, 25 and 50% of Ag, respectively. The $NaBH_4$ solution was added to the suspension, followed by magnetic stirring for 30 minutes. The suspension was then washed several times with ethanol and dried at 80 °C for 18 h.

2.5. Characterization of the prepared materials

2.5.1 X-ray diffraction (XRD). Powder XRD was used to determine the crystallinity of the prepared nanocomposites using a PANalytical X-ray diffractometer (the Netherlands). The X-ray diffractometer possesses a CuKα radiation source with a wavelength of 1.54 Å, a 40 kV accelerating voltage and a 35 mA current.

2.5.2 Fourier transform infrared (FTIR). FTIR spectroscopy was used to study the functional groups in the synthesized Ag/NiO/CNTs nanocomposite. FTIR spectra were recorded using a Vertex-70 (Bruker, Germany).

2.5.3 Electron microscopy imaging. The morphological properties of the composites were studied using a scanning electron microscope (Zeiss Sigma 500 VP) and high-resolution transmission electron microscope (JEOL JEM-2100).

2.5.4 X-ray photoelectron spectroscopy (XPS). XPS analysis was carried out to determine the chemical states and the chemical bonding in the synthesized catalysts. XPS data was recorded using a K-ALPHA (Thermo Fisher Scientific, USA). The instrument possesses a monochromatic Al Kα (200 eV to 4 keV) radiation source that operates at low power ≳72 W and all spectra were recorded at low pressure (10^{-9} mbar). Spectra were acquired within 10 scans (200 seconds for Ni 2p, 90 seconds for O 1s and Ag 3d and 75 seconds for C 1s), with a take-off angle of 50 degree, and a pass energy of 0.1 eV. Data were processed using CasaXPS software by applying a Shirley background subtraction, and then fitting the spectra by applying Voigt functions. All spectra were calibrated by applying a rigid shift to bring the C 1s signal to 284.8 eV, to correct for the shift caused by adventitious carbon.

2.6. Preparation of the working electrodes

A Glassy Carbon (GC) electrode was used as a working electrode with a geometrical surface area of 0.0707 cm^2 to carry out electrochemical measurements. The GC electrode was polished with aqueous alumina suspensions on emery paper until the electrode showed a clean shiny appearance, before washing with DI water, isopropanol, and acetone, sequentially. Then, 5 mg of the prepared nanocomposite were dispersed in a solution containing 400 μL isopropanol and 10 μL Nafion (5%). The catalyst suspension was then sonicated for 30 min before dropping 15 μL of it on the clean GC electrode, three times with a time interval of 5 minutes, until forming a thin layer of the catalyst on the working electrode. Finally, the electrochemical experiments were carried out after the electrode was left to dry under ambient air.

2.7. Electrocatalytic activity measurements

Electrochemical measurements were carried out on a Metrohm Autolab potentiostat (PGSTAT302N) operated using NOVA1.11 software. A conventional three-electrode electrochemical cell containing Ag/AgCl (in saturated KCl solution) acting as the reference electrode, a Pt wire as the counter electrode, and the GC working electrode was used. All electrochemical measurements were carried out, at 25 °C, in 1 M aqueous KOH solution. The current densities of the collected signals were normalized based on the actual electrode geometric surface area (0.0706 cm^2). Cyclic voltammetry (CV) was performed at different scan rates. Electrochemical impedance spectroscopy (EIS) for the different catalysts was measured at 0.7 V and an amplitude of 10 mV. Moreover, stability measurements of the synthesized catalysts were performed using chronoamperometry (CA) at 0.7 V.

3. Results and discussion

3.1. Structural characterization

The crystallinity of different catalysts synthesized here is shown in Fig. 1, which represents the XRD of $Ni(OH)_2$ nano powder, NiO flower-like structure, NiO/CNTs and Ag/NiO/CNTs nanocomposites, respectively. The XRD pattern of the as-prepared $Ni(OH)_2$ precursor is shown in Fig. 1a. All the reflectance peaks can be perfectly indexed to those of a pure phase of $Ni(OH)_2$ with a hexagonal structure. The XRD pattern of the synthesized nickel oxide flower-like structure in Fig. 1b shows diffraction peaks at $2\theta = 37$, 43.5, 62.4, 76, and 79.2 which can be readily indexed as (111), (200), (220), (311), and (222) crystal planes of the NiO, respectively. All the reflections can be indexed to the face-centered cubic (fcc) NiO phase, which agrees well with the standard data (JCPDS card no. 47-1049). The intensity of the peaks indicates the good crystalline nature of the prepared sample. No peaks due to $Ni(OH)_2$ were found from XRD, indicating that $Ni(OH)_2$ was completely decomposed to NiO.

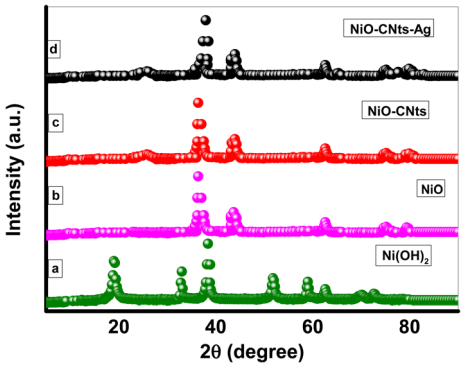

Fig. 1 X-ray diffraction pattern for synthesized nanocomposites. (a) $Ni(OH)_2$, (b) NiO, (c) NiO/CNTs, and (d) Ag/NiO/CNTs.

Furthermore, the successful incorporation of CNTs in the NiO flower-like structure has been evidenced by the broad peak at 2 theta of *ca.* 25.2 in Fig. 1c and d, which is attributed to the (0 0 2) plane of the CNTs.[35] The silver doping of the NiO/CNTs nanocomposite has also been apparent from the peaks at 38.2 and 44.28, which are attributed to the Ag (1 1 1) and Ag (2 0 0) planes, which are fused with the planes of the NiO,[36] as shown in Fig. 1d. Also the 64.440 and 77.340 positions are attributed to the planes of (220), and (311) (JCPDS file no. 04-0783). The Bragg diffraction peaks are shown to be very sharp, thus giving a strong indication of the high crystallinity of the sample and the successful synthesis of NiO nanostructures. Moreover, the XRD peaks of the NiO/CNTs and those of the Ag/NiO/CNTs nanocomposites are similar to those obtained from the NiO, suggesting that doping the NiO with Ag did not affect the sample crystallinity.[37,38] Furthermore, crystallographic parameters are depicted in Table 1 and the crystallite size at different crystallographic planes was calculated using Scherrer's formula. Following Ag and CNT doping, it was discovered that the crystallite size in the NiO sample increased from 16 nm to 32 nm. This crystallite size increase indicates a successful

Table 1 The structural properties of the prepared nanocomposites

Nanocomposite	2-Theta position [°]	Crystallite size [nm]
NiO	38.39	16.22
NiO/CNTs	38.19	22.20
Ag (25%)/NiO/CNTs	38.3813	32.51
Ag (50%)/NiO/CNTs	38.3815	22.13

crystallization process for the NiO/CNTs and the Ag/NiO/CNTs nanocomposite.[39] Interestingly, increasing the Ag (wt%) led to a decrease in the crystallite size, which might be due to inhomogeneous doping (Table 1), consistent with in field emission SEM data analysis of the NiO particles.

3.2. X-ray photoelectron spectroscopy characterization

The survey spectrum for the Ag/NiO/CNTs nanocomposite shows the presence of all the elemental compositions of the nanocomposite (Fig. 2a). The high-resolution Ni 2p spectrum shows a multipeak complex emission (Fig. 2b). The peaks at 857.1 eV and 874.4 eV are attributed to the $2p_{1/2}$ and $2p_{3/2}$ orbitals, respectively, with an area ratio of 2 : 1 and an energy displacement of 17 eV, which correspond to the Ni^{2+} 2p state in the NiO.[40] The peaks at 861.1 and 878.2 eV correspond to the $2p_{1/2}$ and $2p_{3/2}$ orbitals, respectively, with an area ratio of 4 : 2 and a displacement of ~17 eV, which is ascribed to the Ni^{3+} 2p state in the Ni_2O_3.[41] The emissions at 863.1 eV and 869.6 eV are ascribed to the Ni^{2+} 2p satellites; meanwhile, the small emission at 883.2 eV corresponds to the Ni^{3+} 2p satellite, respectively. These results confirm the formation of the NiO nanocomposite, in agreement with previous reports.[42,43] Furthermore, the emission from the Ag 3d orbitals shows two emissions at 367.4 and 373.9 eV that are ascribed to Ag $3d_{5/2}$ and Ag $3d_{3/2}$ with an energy displacement of ~6 eV and an area constraint of 6 : 4, respectively (Fig. 2c).

The emission at 367.4 eV is ascribed to Ag metal in the Ag/NiO/CNTs nanocomposite, and the emission at 373.9 eV is ascribed to the presence of Ag atoms at Ni substitutional atomic sites in the NiO flower-like structure. The slight difference in the peak heights of the core-level of the Ag 3d orbitals suggests that the Ag composition and distribution is uniform in the nanocomposite. It is noteworthy to mention that the appearance of the Ag ions in the XPS, despite the absence of silver phases in the XRD, suggests the formation of an oxidized form of the Ag ions inside the NiO/CNTs flower-like structure. The high-resolution O 1s spectrum in Fig. 2d shows two peaks at 531.2 eV and 532.6 eV that are attributed to the oxygen atom bound to metals (O–Ni) and the oxygen atom coming from other oxygen species such as OH or adventitious CO_2, respectively.

Fig. 2e shows the high-resolution C 1s emission with the emission at 284.3 and 286.5 eV, and 289.8 attributed to the C=O, the C–O, and the C–C orbitals, respectively.[44] The synthesized Ag/NiO/CNTs nanocomposite is a highly crystalline nickel oxide composed of NiO(Ni^{2+}) with traces of a higher oxidation state nickel oxide phase Ni_2O_3(Ni^{3+}) as shown in the XPS analysis.

3.3. Morphological analysis

The morphological and microstructural properties of the synthesized pure NiO and the effect of incorporation of CNTs and Ag on the nanocomposites were characterized using scanning electron microscopy (SEM) and transmission electron microscopy (TEM). Fig. 3a and b show the SEM images of synthesized NiO. The SEM images show the successful formation of a flower-like micro-ball with a hierarchical morphology. All particles have a uniform structure and are mostly of the same size ~5 μm in diameter. Each particle is composed of ~100 nm thick nanoflakes that are arranged in all directions. Fig. 3c and d show the SEM images of the Ag (25%)/NiO/CNTs

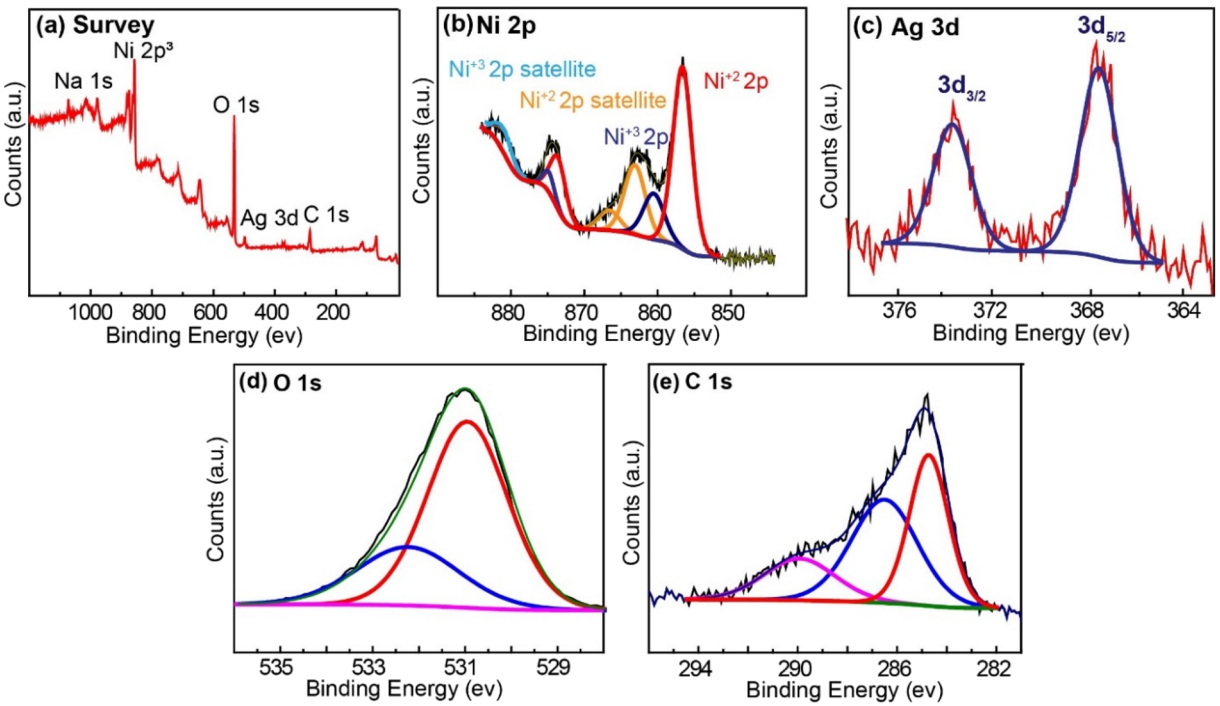

Fig. 2 XPS spectra of Ag (25%)/NiO/CNTs nanocomposites showing the survey spectra with all the elemental compositions in the synthesized nanocomposite (a) and the presence of two different oxidations of Ni, as depicted in the high-resolution Ni 2p emission (b). The high-resolution emission from the silver dopant, oxygen and the carbon is depicted in (c), (d) and (e), respectively.

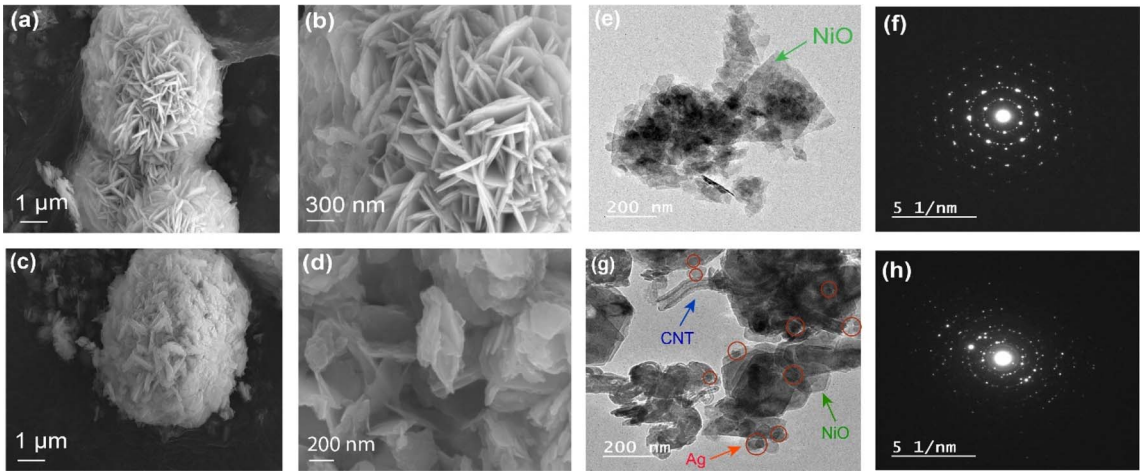

Fig. 3 Electron microscopy imaging for the synthesized catalysts. (a and b) SEM images of NiO nanoflowers with a micro-ball size of ~5 μm. (c and d) SEM images of the Ag (25%)/NiO/CNTs catalyst. (e and f) HRTEM imaging and SAED pattern for the as-synthesized NiO. (g and h) TEM images and SAED of Ag (25%)/NiO/CNTs showing the successful synthesis of the doped catalyst with good crystallinity.

nanocomposites, where it is notably observed that the doping changed the micro-porosity levels and distribution of the micro-balls, with the flakes getting small when CNTs and Ag were incorporated into NiO. In addition, TEM analysis is shown in Fig. 3e for the NiO nanostructure with nanoflakes extending in all directions from the kernel of the 3D hierarchical flower-like structure.

Furthermore, Fig. 3f shows the selected-area electron diffraction (SAED) pattern for the NiO with a hierarchical hexagonal ring structure extending from the kernel of the crystal, demonstrating the crystallinity of the synthesized NiO catalyst. Fig. 3g shows the TEM image for the Ag (25%)/NiO/CNTs where the NiO nanoflakes are transparent, as evidenced by the difference in the image contrast, and the CNTs bridging two nanoflakes with the catalyst are present in a highly poly-crystalline nature, as shown in the SAED pattern in Fig. 3h. It is noteworthy to mention that no Ag is noticed on the exterior surface of Ag/NiO/CNTs in the SEM image (Fig. 3c and d). This is

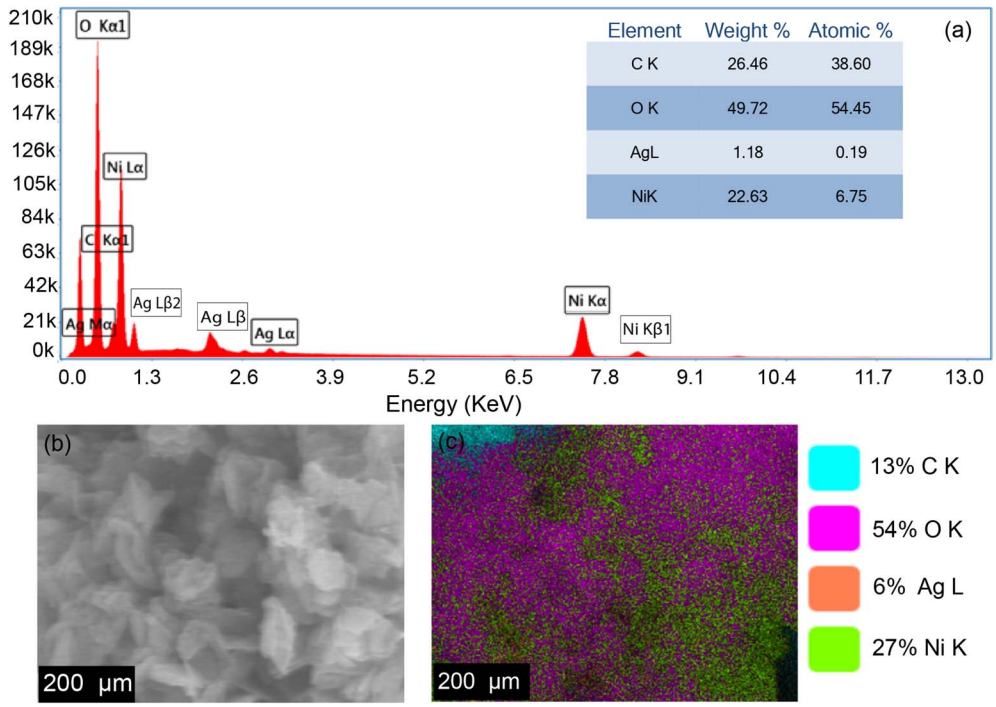

Fig. 4 (a) EDS spectrum of Ag (25%)/NiO/CNTs, the spectrum of Ag (25%)/NiO/CNTs with the atomic and weight percentages are represented in the inset table, (b and c) The elemental mapping images of the Ag (25%)/NiO/CNTs nanocomposite with the elemental compositions homogenously distributed in the image with the Ag atomic : Ni atomic is ~25% : 75% (6 : 27 atomic%).

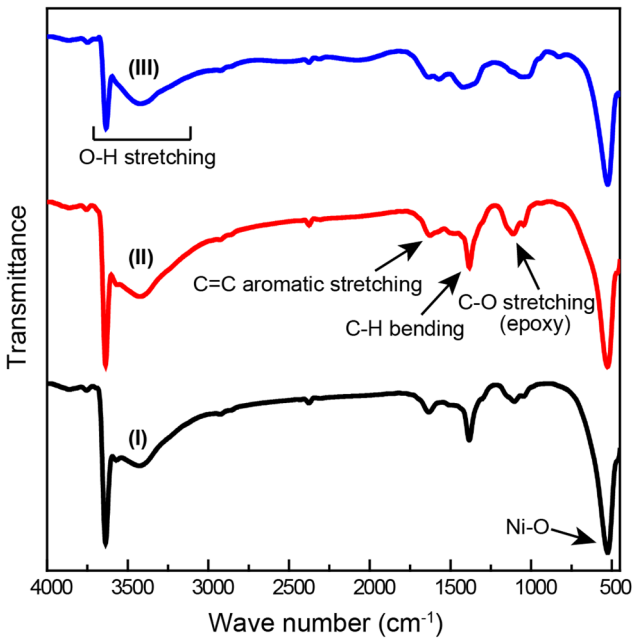

Fig. 5 FTIR spectra of (I) NiO, (II) NiO/CNTs, and (III) Ag/NiO/CNTs showing the functional groups corresponding to CNTs demonstrating the successful formation of the NiO/CNT composite.

probably owing to the possibility that the Ag is mainly decorated into the internal surface of NiO/CNTs between the layered structures. This is consistent with the observation from the TEM images with the uniform distribution of the AgNPs with minimum obvious aggregation. Also, the small size of Ag reveals that the growth of Ag can be controlled by the porous structure of NiO/CNTs during the synthesis process.

Energy dispersive X-ray spectroscopy (EDS) analysis was used to assess the composition and the distribution of the different elements in the synthesized nanocomposite Ag (25%)/NiO/CNTs (Fig. 4). Fig. 4a shows a spectrum representing the weight and atomic ratios of the different elements in the sample, namely, Ni, O, C and Ag with Ni and O contributing to 75% of the elemental weight, followed by C and then by Ag at lower molar weights.

Furthermore, EDS mapping of the Ag (25%)/NiO/CNTs sample shows a uniform distribution of the various elemental compositions (*i.e.*, Ni, O, C and Ag) in the nanocomposite (Fig. 4b and c) with the Ag to Ni ratio of ~0.25 to 0.75 (6% to 27%). These results confirm the successful preparation of the Ag/NiO/CNTs, consistent with the XPS analysis.

Furthermore, FTIR analysis was carried out to determine the surface functional groups and the interlayer anions/cations in the different synthesized nanocomposites. FTIR spectra for the

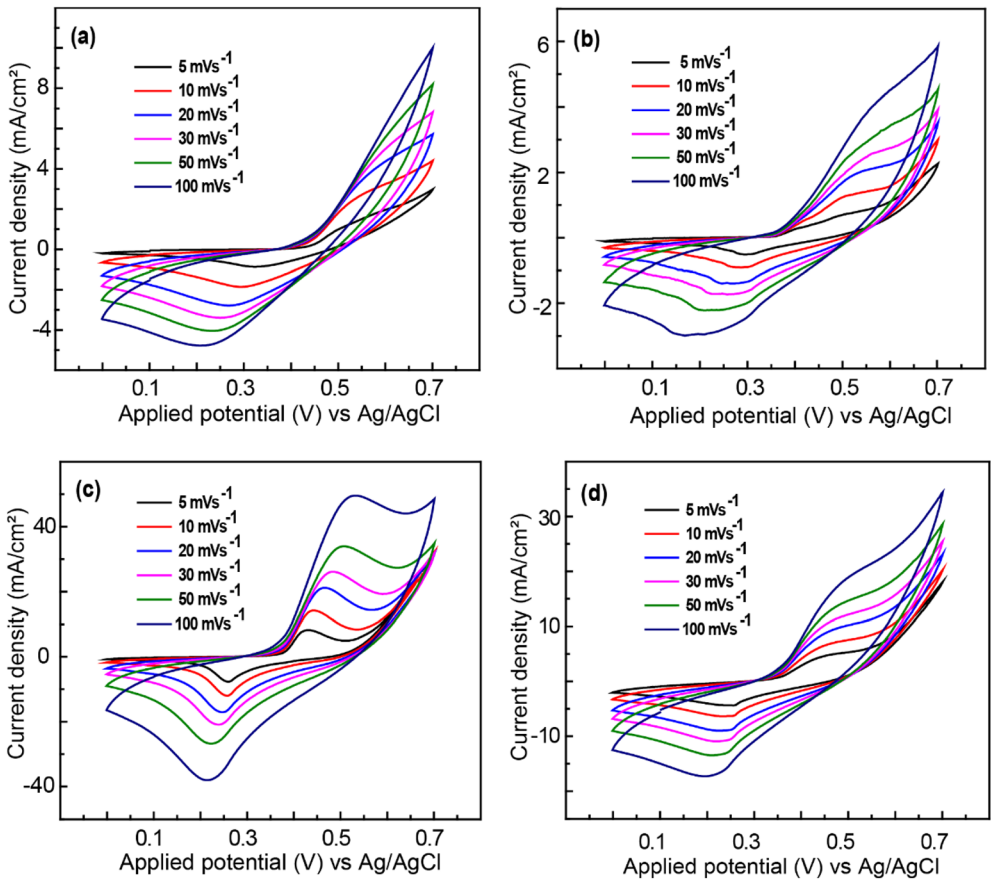

Fig. 6 CVs of the NiO (a), NiO/CNTs (b), Ag (25%)/NiO/CNTs (c) and Ag (50%)/NiO/CNTs (d) at different scan rates at 25 °C. All cyclic voltammetry measurements were carried out in 1 M KOH.

synthesised catalysts NiO, NiO/CNTs and Ag(25%)/NiO/CNTs are shown in Fig. 5I, II and III, respectively.

The vibrational bands observed at 3637 and 3431 cm^{-1} correspond to the O–H stretching of H_2O,[45] which is resulting from the presence of some $Ni(OH)_2$ species. In addition, the weak band near 1635 cm^{-1} is ascribed to C=C aromatic stretching mode.[45,46] The strong absorption peak observed at 1382 cm^{-1} is assigned to the C–H bending and the epoxy group C–O stretching at 1105 cm^{-1}. The peak at 524 cm^{-1} is ascribed to the stretching and bending modes of metal–oxygen (M–O) in the bonding, which indicates the frequency of the Ni–O bond bending vibrations.[46] Therefore, FTIR analysis, together with electron microscopy and XRD, confirms the formation of NiO in a composite form with the carbon nanotubes, which is decorated with Ag.

3.4. Electrocatalytic activity

The electrochemical behaviors of the prepared nanocomposite catalysts were studied using cyclic voltammetry (CV) in 1 M KOH between 100 and 700 mV (*vs.* Ag/AgCl reference electrode). CV curves in Fig. 6 show two symmetrical redox peaks for all tested nanocomposites (NiO, NiO/CNTs, and Ag/NiO/CNTs). These redox peaks are attributed to the oxidation of NiO to NiOOH (eqn (1)), which corresponds to the faradaic reaction of nickel oxide in basic media.

$$NiO + OH^- \leftrightarrow NiOOH + H_2O + e^- \quad (1)$$

Moreover, it was found that, in alkali media, NiO based catalysts have a different behavior where their hydroxyl groups enter the interlayer easily with a higher mobility, in contrast to the other anions in the electrolyte solution. The current density for hybrid nanocomposites increases to a higher value compared to the pure NiO, which could be due to the 2D multifunctional materials (CNTs) formed, which determines a higher number of active sites for reaction.

This enhancement in current density agrees with the structural and morphological properties obtained with TEM results (Fig. 3), which confirm that Ag was uniformly doped in NiO/CNTs without introducing structural collapse or aggregation, forming a new 3D multifunctional structure with higher electrochemical activity.

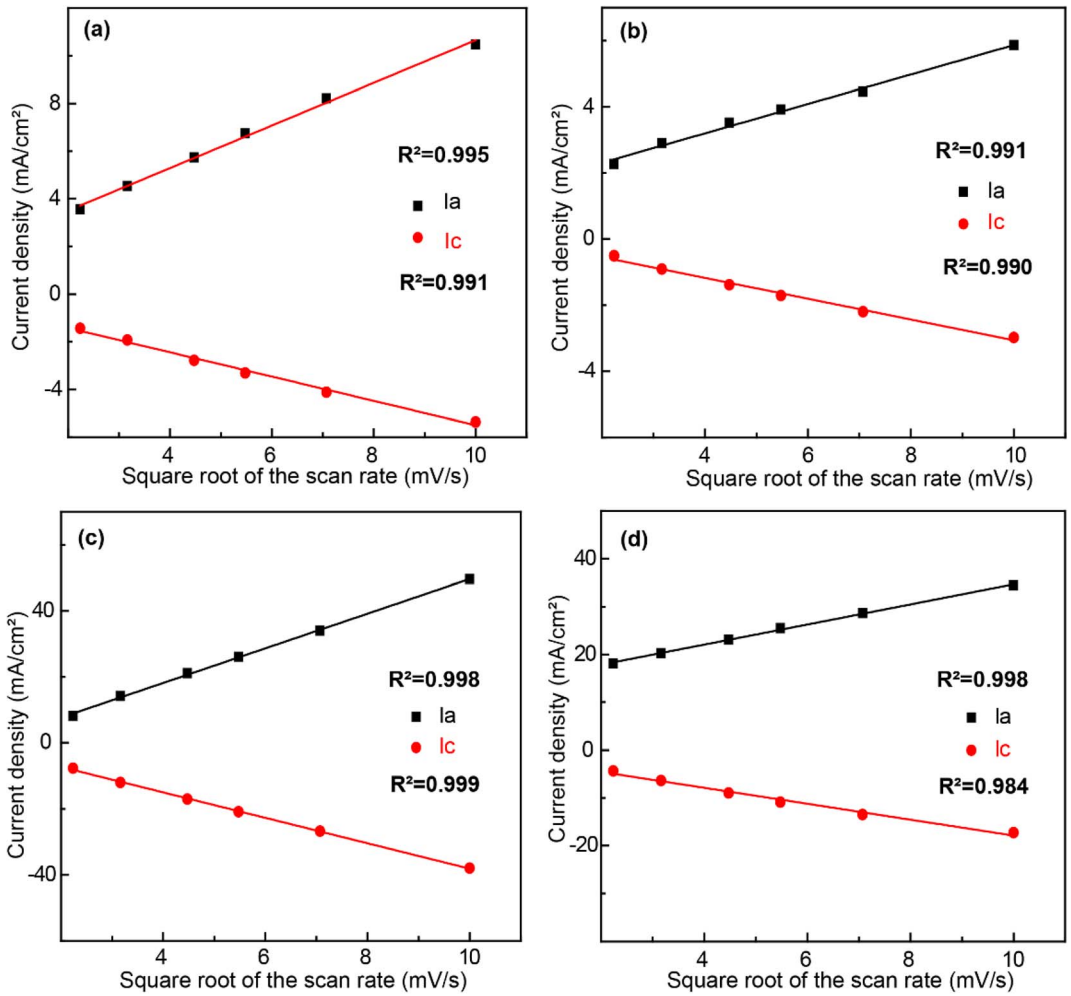

Fig. 7 The evolution of the square root of the scan rate *versus* the peak currents (anodic and cathodic) for the synthesized nanocomposites, namely, NiO (a), NiO/CNTs (b), Ag (25%)/NiO/CNTs (c) and Ag (50%)/NiO/CNTs (d).

The evolution of the cathodic and the anodic peak currents is linearly proportional to the square root of the scan rate (Fig. 7), suggesting that the diffusion of the OH^- ions into the pores of the NiO-based nanocomposites controls the redox process at the electrode/electrolyte. This in turn enhances the catalytic activity of the material.

The hybridization of NiO/CNTs and Ag can give a new synergistic effect as a new category of ethanol electro-oxidation catalysts. The electro-catalytic activity of NiO/CNTs and Ag (25%)/NiO/CNTs nanocomposites for ethanol electro-oxidation was studied using CV. The CV curves were measured in the presence of different ethanol concentrations of 0.1, 0.3, 0.5, 1, 2 and 3 mol L^{-1}. Fig. 8 illustrates the CV at 50 mV s^{-1} in the potential window from −100 to 800 mV for NiO, NiO/CNTs and Ag/NiO/CNTs. The results show an increase in the current density with increasing ethanol concentrations for all the nanocomposites, which indicates the increased ethanol electro-oxidation when more ethanol was made available. The catalytic activity for the NiO was found to be active for only one concentration of ethanol (0.1 mol L^{-1}) (Fig. 8a); meanwhile, immobilizing the NiO on a supporting material (CNTs) resulted in an increase in the ethanol concentration uptake by the new catalyst (NiO/CNTs) to 0.3 mol L^{-1} (Fig. 8b) and the faradaic current in the range of 12 mA cm^{-2}.

Furthermore, doping the NiO/CNTs nanocomposite with Ag led to a huge increase in the faradaic current of the new nanocomposite Ag (25%)/NiO/CNTs, with the current increasing from 12 mA cm^{-2} to 50 mA cm^{-2} at 0.1 mol per L ethanol (Fig. 8c). The catalytic activity of the synthesized Ag (25%)/NiO/CNTs electrocatalyst is attributed to the active site of the NiO, which involves the conversion of the Ni^{2+} to Ni^{3+}. However, the presence of the noble metal (Ag) introduces an extra synergetic electronic effect that accelerates the catalytic rate determining step.[47–49] The decrease in the electrocatalytic activity with increasing the Ag ratio above 25% could be attributed to the metal-induced toxicity for the Ni-based active sites, which leads to a drop in the catalytic activity. This demonstrates a higher fuel conversion efficiency with achieving a significantly higher current at 0.1 mol per L ethanol, which is five-fold higher than the current obtained from 1 mol per L ethanol, under the same alkaline conditions, oxidized on the Pd–NiO/C catalyst, and three-fold higher than a mixture of NiO and ZrO_2 supported with reduced graphene oxide (Table 2). In addition, Table 2 shows a further comparison of the Ag/NiO/

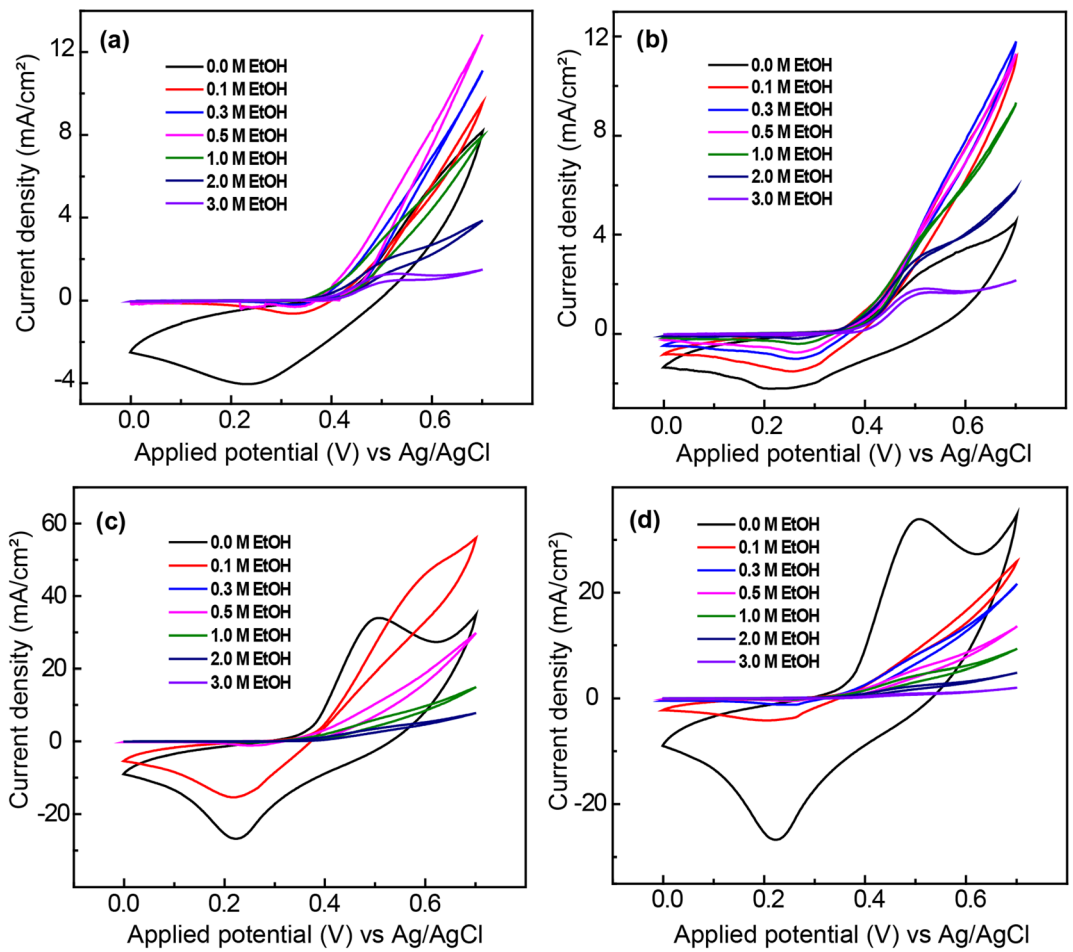

Fig. 8 CVs of the NiO (a), NiO/CNTs (b), Ag (25%)/NiO/CNTs (c) and Ag (50%)/NiO/CNTs (d) at different ethanol concentrations at 50 mV s^{-1} scan rate. All cyclic voltammetry measurements were carried out in 1 M KOH.

Table 2 Comparison of current densities of different NiO-based catalysts toward the ethanol electro-oxidation reaction

Anode catalyst	Ethanol concentration (M)	Electrolyte	Scan rate (mV s^{-1})	Current density (mA cm^{-2})	Reference
Ag/NiO/CNTs	0.1	1 M KOH	50	56.40	This work
NiO-f/GCE	0.1	1 M NaOH	50	3.50	50
NiO/G-C-15	1.0	0.5 M NaOH	10	21.59	51
Pt–MWCNT–NiO	1.0	0.5 M NaOH	25	12.50	52
Pd–NiO	3.0	0.3 M KOH	20	24.98	53
Pd–NiO/C	1.0	1 M KOH	50	11.50	54
ZrO_2/NiO/rGO	0.5	0.5 M KOH	20	17.30	55
MnO_2–NiO–MWCNTs	0.5	1 M KOH	50	0.148	56

CNTs catalyst with a series of NiO-based catalysts used for ethanol oxidation published in similar studies and this work on the Ag/NiO/CNTs nanocomposite results in the highest current per ethanol concentration.

Increasing the concentration of the Ag to 50% did not enhance the catalytic activity of the Ag/NiO/CNTs composite but conversely led to a lower faradaic current and a lower ethanol conversion capacity (0.1 mol L^{-1}) (Fig. 8d). However, while 25% doping leads to establishing a conductive network with better electron transport properties, higher doping ratios of Ag might be affecting the crystallinity and thus disturbing electron transfer pathways. This is also consistent with the decrease of the crystallite size with the 50% doping observed in the XRD data. In addition, the 3D structures of the Ag (25%)/NiO/CNTs play an important role in preventing aggregation and providing electrolyte percolation to achieve high accessibility for the active area.

It is noteworthy to mention that the onset potential in the CV was shifted towards more negative values, with increasing the ethanol concentrations until the surface reached the maximum conversion of ethanol at 0.3 mol L^{-1} for all the nanocomposites (Fig. 9). It was also found that increasing the ethanol concentration above 0.3 mol L^{-1} led to a decrease in the faradaic current and reversed the onset potential towards more positive values, indicating that the surface has reached a maximum catalytic activity.

Fig. 9a and b show the change in the onset potential values for the different nanocomposites with 0.3 mol per L ethanol in alkaline media (1 M KOH). The onset potential was found to shift towards more negative values, accompanied by an increase in the faradaic current, and the highest negative shift was observed for the Ag (25%)/NiO/CNTs sample.

This suggests that decorating the surface of the NiO flower-like structure with highly catalytic silver boosted the catalytic activity by one order of magnitude while keeping an excellent crystallinity, consistent with the XRD patterns in Fig. 1.

Although the mechanism of ethanol oxidation is more complicated than that of methanol, and it is unclear yet what the possible ethanol oxidation routes on the surface of the electrocatalyst are, ethanol has been suggested to undergo electrochemical oxidation *via* the following scheme:[57]

$$CH_3CH_2OH \rightleftharpoons CH_3CH_2OH_{ad} \quad (2)$$

$$CH_3CH_2OH_{ad} \rightarrow CO_{ad} + CH_{x,ad} + (6-x)H^+ + (6-x)e^- \quad (3)$$

$$CH_3CH_2OH_{ad} \rightarrow CH_3CHO_{ad} + 2H^+ + 2e^- \quad (4)$$

$$CH_3CHO_{ad} \rightleftharpoons CH_3CHO \quad (5)$$

$$CH_3CHO_{ad} \rightarrow CO_{ad} + CH_{x,ad} + (4-x)H^+ + (4-x)e^- \quad (6)$$

$$H_2O \rightarrow OH_{ad} + H^+ + e^- \quad (7)$$

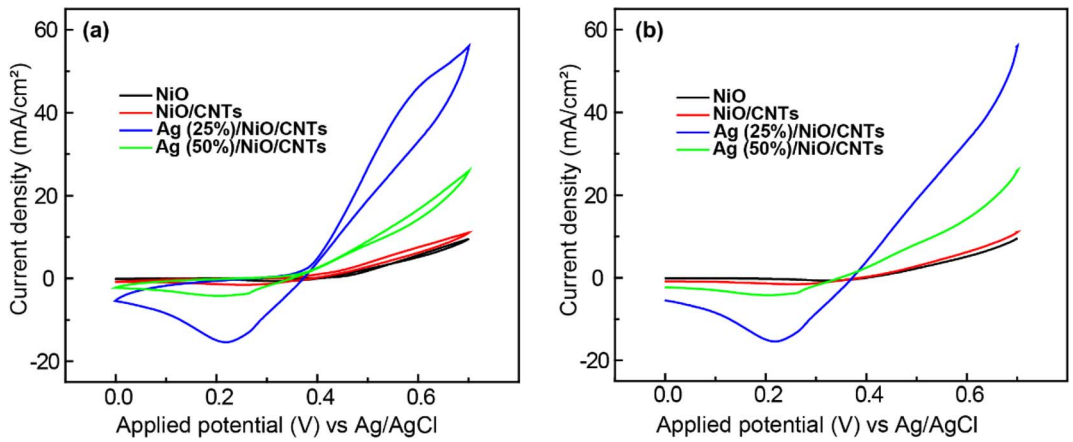

Fig. 9 (a) CVs of the NiO, NiO/CNTs, Ag (25%)/NiO/CNTs and Ag (50%)/NiO/CNTs and (b) its corresponding onset potential with 0.1 mol per L ethanol at a scan rate of 50 mV s^{-1}.

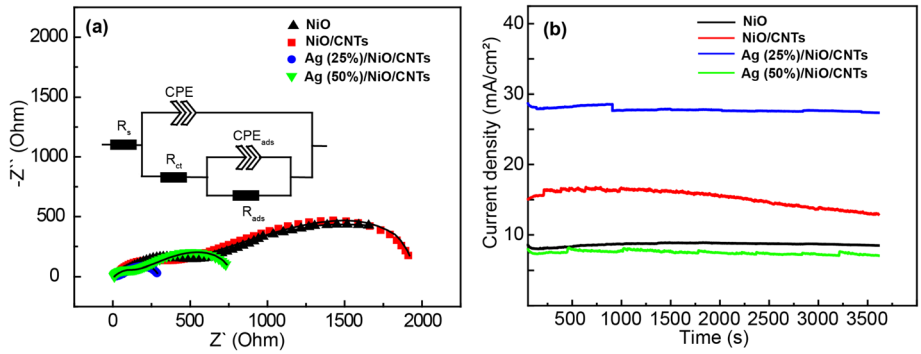

Fig. 10 (a) Nyquist plots for the ethanol oxidation reaction of the different NiO nanocomposites at 0.1 mol per L ethanol in 1 M KOH. (b) Chronoamperometric response for the different nanocomposites at 0.35 V *vs.* Ag/AgCl reference electrode at 0.1 M ethanol in 1 M KOH.

Table 3 Values of the electrochemical impedance fitted to the equivalent electric circuit

			CPE			CPE_{ads}	
Sample ID	R_s	R_{ct}	CPE T	CPE P	R_{ads}	CPE T	CPE P
NiO	19.4	425	2.6×10^{-6}	0.73	477	7.39×10^{-5}	0.67
NiO/CNTs	27.3	348	4.5×10^{-6}	0.71	912	2.97×10^{-4}	0.51
AgNPs (25%)/NiO/CNTs	11.1	135	1.8×10^{-3}	0.69	58.1	1.57×10^{-3}	0.35
AgNPs (50%)/NiO/CNTs	8.45	125	2.2×10^{-5}	0.79	693	7.39×10^{-4}	0.67

$$CH_3CHO_{ad} + OH_{ad} \rightarrow CH_3COOH + H^+ + e^- \quad (8)$$

$$CO_{ad} + OH_{ad} \rightarrow CO_2 + H^+ + e^- \quad (9)$$

$$CH_{x,ad} + 2OH_{ad} \rightarrow CO_2 + (2 - x)H^+ + (2 - x)e^- \quad (10)$$

Ethanol oxidation starts with the OH group splitting to an H^+ and an ethoxy group (CH_2CH_3O). The CH_2CH_3O is then converted to acetaldehyde species which is then oxidized to many other possible species including acetate, carbon dioxide, carbon monoxide and other hydrocarbons.

3.5. Electrochemical impedance spectroscopy (EIS)

Fig. 10a displays the electrochemical impedance spectroscopy (EIS) recorded in 1 M KOH containing 0.1 mol per L ethanol at 0.35 V *vs.* Ag/AgCl reference electrode. The Nyquist plot of the EIS obtained from the different electrocatalysts (NiO, NiO/CNTs, Ag (25%)/NiO/CNTs and Ag (50%)/NiO/CNTs) and the equivalent electrochemical circuit are represented in Fig. 10a. The electrochemical equivalent circuit consists of two parts. The first part includes the electrolyte's resistance represented by R_s, constant phase element (CPE) and the charge transfer resistance (R_{ct}). The second part is composed of an adsorption related constant phase element (CPE_{ads}) and the resistance obtained from the intermediate adsorption rate (R_{ads}). The different electrocatalysts have shown various electrochemical impedances with R_{ct} values of 425 Ohm for NiO and 348, 135, and 125 for NiO/CNTs, Ag (25%)/NiO/CNTs and Ag (50%)/NiO/CNTs, respectively (Table 2). The charge transfer resistance data (Table 3) agrees with the CV measurements, illustrating that NiO has shown the highest resistance and that the resistance of the NiO slightly decreased upon adding CNTs. Doping with Ag led to a significant improvement in the material conductance and consequently its electrocatalytic activity, demonstrated by the very low impedance of the Ag (25%)/NiO/CNTs sample. The electrochemical stability of the as-synthesized NiO nanocomposites was tested using chronoamperometric measurements at 0.35 V *vs.* Ag/AgCl reference for 1 hour. Fig. 10b shows the evolution of the current decay, with all the materials showing no significant current decay (<10%) over the testing period (1 h). This adds a stronger merit to the synthesized electrocatalysts here due to the lack of stability of most of the commercially available metallic catalysts that suffer from the fast accumulation of carbonaceous intermediates such as carbon monoxide (CO), which led to fast catalyst poisoning.

4. Conclusion

Here, different nickel oxide (NiO)-based nanocomposite electrocatalysts were synthesized using a hydrothermal method. The different nanocomposites showed excellent electrocatalytic activity for ethanol oxidation. The stability of the NiO was improved by forming a nanocomposite with carbon nanotubes (CNTs), and meanwhile the electrocatalytic performance towards ethanol oxidation was boosted when the NiO/CNTs nanocomposite was decorated with silver (Ag). Moreover, the ratio of Ag doping was found to be very critical, with the maximum ethanol oxidation capacity and the highest faradaic current obtained using 25% (wt%) of Ag. The Ag (25%)/NiO/CNTs showed a maximum ethanol conversion. At an ethanol concentration of 300 mM, the electrochemical oxidation current

density of Ag (25%)/NiO/CNTs (57.1 ± 0.2 mA cm^{-2}) was found to increase by five times compared to the current density of the NiO/CNTs (10 ± 0.34 mA cm^{-2}). This work opens a realm of opportunities for designing new electrochemical catalysts for ethanol oxidation, which in turn paves the way for direct ethanol fuel cells as safer and more eco-friendly energy sources.

Data availability

The data that have been used is confidential.

Conflicts of interest

There are no conflicts to declare.

References

1 O. Edenhofer, *et al.*, On the economics of renewable energy sources, *Energy Econ.*, 2013, **40**, S12–S23.
2 O. Edenhofer, *et al.*, *Renewable Energy Sources and Climate Change Mitigation: Special Report of the Intergovernmental Panel on Climate Change*, Cambridge University Press, 2011.
3 S. Jenniches, Assessing the regional economic impacts of renewable energy sources – A literature review, *Renewable Sustainable Energy Rev.*, 2018, **93**, 35–51.
4 R. A. Sayed, *et al.*, Co-Fe layered double hydroxide decorated titanate nanowires for overall photoelectrochemical water splitting, *J. Alloys Compd.*, 2017, **728**, 1171–1179.
5 M. Z. F. Kamarudin, *et al.*, Review: Direct ethanol fuel cells, *Int. J. Hydrogen Energy*, 2013, **38**(22), 9438–9453.
6 E. Berretti, *et al.*, Direct Alcohol Fuel Cells: A Comparative Review of Acidic and Alkaline Systems, *Electrochem. Energy Rev.*, 2023, **6**(1), 30.
7 S. Sundarrajan, S. I. Allakhverdiev and S. Ramakrishna, Progress and perspectives in micro direct methanol fuel cell, *Int. J. Hydrogen Energy*, 2012, **37**(10), 8765–8786.
8 X. Ren, *et al.*, Methanol transport through nation membranes. electro-osmotic drag effects on potential step measurements, *J. Electrochem. Soc.*, 2000, **147**(2), 466.
9 N. W. Deluca and Y. A. Elabd, Polymer electrolyte membranes for the direct methanol fuel cell: a review, *J. Polym. Sci., Part B: Polym. Phys.*, 2006, **44**(16), 2201–2225.
10 T. S. Zhao, *et al.*, Mass transport phenomena in direct methanol fuel cells, *Prog. Energy Combust. Sci.*, 2009, **35**(3), 275–292.
11 H. Liu, *et al.*, A review of anode catalysis in the direct methanol fuel cell, *J. Power Sources*, 2006, **155**(2), 95–110.
12 K. Elsaid, *et al.*, Direct alcohol fuel cells: Assessment of the fuel's safety and health aspects, *Int. J. Hydrogen Energy*, 2021, **46**(59), 30658–30668.
13 S. P. S. Badwal, *et al.*, Direct ethanol fuel cells for transport and stationary applications – A comprehensive review, *Appl. Energy*, 2015, **145**, 80–103.
14 L. An, T. S. Zhao and Y. S. Li, Carbon-neutral sustainable energy technology: Direct ethanol fuel cells, *Renewable Sustainable Energy Rev.*, 2015, **50**, 1462–1468.
15 Y. H. Chu and Y. G. Shul, Combinatorial investigation of Pt–Ru–Sn alloys as an anode electrocatalysts for direct alcohol fuel cells, *Int. J. Hydrogen Energy*, 2010, **35**(20), 11261–11270.
16 B. D. McNicol, D. A. J. Rand and K. R. Williams, Fuel cells for road transportation purposes — yes or no?, *J. Power Sources*, 2001, **100**(1), 47–59.
17 G. Andreadis and P. Tsiakaras, Ethanol crossover and direct ethanol PEM fuel cell performance modeling and experimental validation, *Chem. Eng. Sci.*, 2006, **61**(22), 7497–7508.
18 F. Colmati, E. Antolini and E. R. Gonzalez, Effect of temperature on the mechanism of ethanol oxidation on carbon supported Pt, PtRu and Pt3Sn electrocatalysts, *J. Power Sources*, 2006, **157**(1), 98–103.
19 M. Amani, *et al.*, Investigation of methanol oxidation on a highly active and stable Pt–Sn electrocatalyst supported on carbon–polyaniline composite for application in a passive direct methanol fuel cell, *Mater. Res. Bull.*, 2015, **68**, 166–178.
20 K. Wang, *et al.*, Surface-tailored PtPdCu ultrathin nanowires as advanced electrocatalysts for ethanol oxidation and oxygen reduction reaction in direct ethanol fuel cell, *J. Energy Chem.*, 2021, **52**, 251–261.
21 R. M. Altarawneh, Overview on the Vital Step toward Addressing Platinum Catalyst Poisoning Mechanisms in Acid Media of Direct Ethanol Fuel Cells (DEFCs), *Energy Fuels*, 2021, **35**(15), 11594–11612.
22 S. Kumar, *et al.*, 14 – Metal oxides for energy applications, in *Colloidal Metal Oxide Nanoparticles*, ed. S. Thomas, A. Tresa Sunny and P. Velayudhan, Elsevier, 2020, pp. 471–504.
23 V. Vij, *et al.*, Nickel-Based Electrocatalysts for Energy-Related Applications: Oxygen Reduction, Oxygen Evolution, and Hydrogen Evolution Reactions, *ACS Catal.*, 2017, **7**(10), 7196–7225.
24 U. K. Chime, *et al.*, Recent progress in nickel oxide-based electrodes for high-performance supercapacitors, *Curr. Opin. Electrochem.*, 2020, **21**, 175–181.
25 Y. Tang, *et al.*, Hydrothermal synthesis of a flower-like nano-nickel hydroxide for high performance supercapacitors, *Electrochim. Acta*, 2014, **123**, 158–166.
26 C. D. Gu, *et al.*, NiO electrode for methanol electro-oxidation: Mesoporous vs. nanoparticulate, *Int. J. Hydrogen Energy*, 2014, **39**(21), 10892–10901.
27 J. Chen, *et al.*, Recent developments of nanocarbon based supports for PEMFCs electrocatalysts, *Chin. J. Catal.*, 2021, **42**(8), 1297–1326.
28 C. Hu, *et al.*, Carbon Nanomaterials for Energy and Biorelated Catalysis: Recent Advances and Looking Forward, *ACS Cent. Sci.*, 2019, **5**(3), 389–408.
29 M. A. Nassar, *et al.*, Highly efficient asymmetric supercapacitor-based on Ni-Co oxides intercalated graphene as positive and Fe2O3 doped graphene as negative electrodes, *J. Energy Storage*, 2021, **44**, 103305.
30 L. M. Esteves, H. A. Oliveira and F. B. Passos, Carbon nanotubes as catalyst support in chemical vapor deposition reaction: A review, *J. Ind. Eng. Chem.*, 2018, **65**, 1–12.

31 T. T. T. L. Hoang, N. Insin and N. Sukpirom, Catalytic activity of silver nanoparticles anchored on layered double hydroxides and hydroxyapatite, *Inorg. Chem. Commun.*, 2020, **121**, 108199.
32 M. S. Abdel-wahab, H. K. El Emam and W. M. El Rouby, Sputtered Ag-doped NiO thin films: structural, optical, and electrocatalytic activity toward methanol oxidation, *J. Mater. Sci.: Mater. Electron.*, 2023, **34**(22), 1637.
33 S. Yin, *et al.*, Flower-like NiO with a Hierarchical and Mesoporous Structure for Supercapacitors, *ChemElectroChem*, 2017, **4**(10), 2563–2570.
34 Q. Bin, M. Wang and L. Wang, Ag nanoparticles decorated into metal-organic framework (Ag NPs/ZIF-8) for electrochemical sensing of chloride ion, *Nanotechnology*, 2020, **31**(12), 125601.
35 C. E. Kozonoe, R. Giudici and M. Schmal, Ruthenium catalyst supported on multi-walled carbon nanotubes for CO oxidation, *Mod. Res. Catal.*, 2021, **10**(3), 73–91.
36 P. Sistani, *et al.*, A Penicillin Biosensor by Using Silver Nanoparticles, *Int. J. Electrochem. Sci.*, 2014, **9**(11), 6201–6212.
37 W. Lee, *et al.*, Synthesis of Ni/NiO core-shell nanoparticles for wet-coated hole transport layer of the organic solar cell, *Surf. Coat. Technol.*, 2013, **231**, 93–97.
38 M. Praveen Kumar, *et al.*, NiFe Layered Double Hydroxide Electrocatalyst Prepared via an Electrochemical Deposition Method for the Oxygen Evolution Reaction, *Catalysts*, 2022, **12**(11), 1470.
39 D. Deep Yadav, *et al.*, Synthesis and characterisation of Nickel oxide nanoparticles using CTAB as capping agent, *Mater. Today: Proc.*, 2023, **73**, 333–336.
40 G. Wang, *et al.*, A mechanistic study into the catalytic effect of Ni(OH)2 on hematite for photoelectrochemical water oxidation, *Nanoscale*, 2013, **5**(10), 4129–4133.
41 A. Davidson, *et al.*, Spectroscopic studies of nickel (II) and nickel (III) species generated upon thermal treatments of nickel/ceria-supported materials, *J. Phys. Chem.*, 1996, **100**(12), 4919–4929.
42 A. P. Grosvenor, *et al.*, New interpretations of XPS spectra of nickel metal and oxides, *Surf. Sci.*, 2006, **600**(9), 1771–1779.
43 M. S. Abdel-wahab, H. K. El Emam and W. M. A. El Rouby, Sputtered Ag-doped NiO thin films: structural, optical, and electrocatalytic activity toward methanol oxidation, *J. Mater. Sci.: Mater. Electron.*, 2023, **34**(22), 1637.
44 P. Hong, *et al.*, Efficient generation of singlet oxygen (1O2) by hollow amorphous Co/C composites for selective degradation of oxytetracycline via Fenton-like process, *Chem. Eng. J.*, 2021, **421**, 129594.
45 P. Vijaya Kumar, A. Jafar Ahamed and M. Karthikeyan, Synthesis and characterization of NiO nanoparticles by chemical as well as green routes and their comparisons with respect to cytotoxic effect and toxicity studies in microbial and MCF-7 cancer cell models, *SN Appl. Sci.*, 2019, **1**(9), 1083.
46 A. A. Ezhilarasi, *et al.*, Green synthesis of NiO nanoparticles using Moringa oleifera extract and their biomedical applications: Cytotoxicity effect of nanoparticles against HT-29 cancer cells, *J. Photochem. Photobiol., B*, 2016, **164**, 352–360.
47 C. Liu, *et al.*, Recent progress of Ni-based catalysts for methanol electrooxidation reaction in alkaline media, *Advanced Sensor and Energy Materials*, 2023, **2**(2), 100055.
48 C. Liu, *et al.*, An active Ni(OH)2/MnCO3 catalyst with efficient synergism for alkaline methanol oxidation, *Chem. Commun.*, 2024, **60**(12), 1591–1594.
49 M. Li, *et al.*, MoP-NC Nanosphere Supported Pt Nanoparticles for Efficient Methanol Electrolysis, *Acta Phys.-Chim. Sin.*, 2023, 2301005.
50 J. Zhan, *et al.*, Boosting ethanol oxidation over nickel oxide through construction of quasi-one-dimensional morphology and hierarchically porous structure, *Trans. Nonferrous Met. Soc. China*, 2020, **30**(6), 1615–1624.
51 R. M. Abdel Hameed, Nickel Oxide Nanoparticles Supported on Graphitized Carbon for Ethanol Oxidation in NaOH Solution, *J. Cluster Sci.*, 2019, **30**(4), 1003–1016.
52 A. S. Adekunle, *et al.*, Ethanol Sensor Based On Platinum-MWCNT-NiO Nanoparticles Platform Electrode, *Int. J. Electrochem. Sci.*, 2012, **7**(3), 2695–2709.
53 C. A. López-Rico, *et al.*, High performance of ethanol co-laminar flow fuel cells based on acrylic, paper and Pd-NiO as anodic catalyst, *Electrochim. Acta*, 2016, **207**, 164–176.
54 F. Hu, *et al.*, Mechanistic study of ethanol oxidation on Pd–NiO/C electrocatalyst, *Electrochim. Acta*, 2006, **52**(3), 1087–1091.
55 M. B. Askari, H. Beitollahi and A. Di Bartolomeo, Methanol and Ethanol Electrooxidation on ZrO(2)/NiO/rGO, *Nanomaterials*, 2023, **13**(4), 679.
56 M. Shojaeifar, *et al.*, MnO2–NiO–MWCNTs nanocomposite as a catalyst for methanol and ethanol electrooxidation, *J. Phys. D: Appl. Phys.*, 2022, **55**, 355502.
57 O. Guillén-Villafuerte, *et al.*, New insights on the electrochemical oxidation of ethanol on carbon-supported Pt electrode by a novel electrochemical mass spectrometry configuration, *Electrochem. Commun.*, 2016, **63**, 48–51.